Additive Manufacturing 73 (2023) 103681

Contents lists available at ScienceDirect

Additive Manufacturing

journal homepage: www.elsevier.com/locate/addma

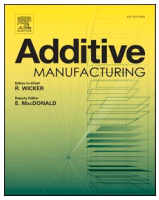

A novel cold wire gas metal arc (CW-GMA) process for high productivity additive manufacturing

Chong Wang *, Jun Wang, João Bento, Jialuo Ding, Goncalo Pardal, Guangyu Chen, Jian Qin, Wojciech Suder, Stewart Williams *

Welding and Additive Manufacturing Centre, Cranfield University, Bedfordshire MK43 0AL, UK

ARTICLE INFO

Keywords:
Wire-arc DED
High deposition rate
Process model
Microstructure
Mechanical properties

ABSTRACT

Wire-arc directed energy deposition (DED) is suitable for depositing large-scale metallic components at high deposition rates. In order to further increase productivity and efficiency by reducing overall manufacturing time, higher deposition rates are desired. However, the conventional gas metal arc (GMA) based wire-arc DED, characterised by high energy input, normally results in high remelting and reheating at relatively high deposition rates, reducing the process efficiency and deteriorating the mechanical performance. In this study, a novel wire-arc DED process with the combination of a GMA and an external cold wire, namely cold wire-gas metal arc (CW-GMA), was proposed for achieving high deposition rate and low material remelting. The maximum deposition rates at different levels of energy input were investigated, with the highest deposition rate of 14 kg/h being achieved. An industrial-scale component weighing 280 kg was built with this process at a high deposition rate of around 10 kg/h, which demonstrated the capability of the process for high productivity application. It was also found that, due to the addition of the cold wire, the remelting was reduced significantly. The working envelope and geometric process model for the CW-GMA process was developed, which can be used to avoid defects in parameter selection and predict the geometry of single-pass wall structures. Moreover, the addition of the cold wire in the CW-GMA process reduced the specific energy density, leading to a reduction in both grain size and anisotropy, which improved the mechanical properties with increased strength and reduced anisotropy.

1. Introduction

Additive manufacturing (AM), also known as 3D printing, is a transformative technology that presents numerous advantages over traditional manufacturing techniques, such as higher design flexibility, faster time-to-market, reduced waste, customisation, and enhanced efficiency [1–3]. Wire-arc directed energy deposition (DED), as a significant branch of AM, employs an electric arc as a heat source and metallic wire as feedstock, which facilitates the construction of large metallic components on a scale of meters [4–6]. Among the various electric arc types applicable in wire-arc DED, gas metal arc (GMA) stands out due to its consumable electrode, which contributes to higher energy transfer efficiency compared to non-consumable types such as gas tungsten arc (GTA) and plasma transferred arc (PTA). In addition, it has higher tolerance in terms of the path planning and omnidirectionality compared to the GTA and PTA processes, owing to a coaxial configuration of wire and torch [3]. As a result, GMA is a preferred option for material deposition, whenever feasible.

So far, with a single GMA, a deposition rate of 3 kg/h is achievable with a good surface finish for steel [4]. Higher deposition rates are often required in practical production to reduce the lead time and overall costs. For example, in mining and construction industries, the components can weigh up to several tonnes. To make the process viable for large components like this, the deposition rate needs to be increased significantly. However, a higher deposition rate can be achieved but at the cost of low surface quality and dimensional accuracy, which means a large amount of material needs to be machined off, reducing the cost-effectiveness of the process. Examples can be seen with the tandem process [7] and dual plasma process [8], where high deposition rates were achieved but with reduced resolution and precision of the components. This is because the surface finish and geometric accuracy are dictated by the process stability and the melt pool behaviour, which are more difficult to control at higher deposition rates [9].

Another factor that restricts the high deposition rate with the GMA

* Corresponding authors.
E-mail addresses: chong.wang1@cranfield.ac.uk (C. Wang), s.williams@cranfield.ac.uk (S. Williams).

https://doi.org/10.1016/j.addma.2023.103681
Received 24 March 2023; Received in revised form 6 June 2023; Accepted 27 June 2023
Available online 29 June 2023

based wire-arc DED is high remelting. The high energy input of the process at high deposition rate results in a high remelting on the substrate or pre-deposited layers, which reduces the process efficiency and deteriorates the mechanical performance. This is because in the standard GMA process (i.e., GMA process without cold wire feeding), the energy input is directly coupled with the material feeding rate. The remelting is increased along with the material feeding rate (or energy input). In fact, as a variant of GMA, cold metal transfer (CMT) technique provides a controlled method of material deposition and low thermal input, which does not have the high remelting issue [10]. However, the deposition rate in this process is relatively low due to the speed limit of the wire feed. Therefore, in this study, to increase the deposition rate while maintaining a low remelting, an external non-energised cold wire was added to the GMA, namely cold wire-GMA (CW-GMA). In this process, the cold wire is fed to the GMA and takes energy from it. By doing this, more feedstock can be melted with the same amount of energy input, and the energy input can be decoupled from the material feeding rate. Therefore, it is expected that the deposition rate can be improved and the remelting can be reduced, leading to a high productivity and high quality process.

To date, the CW-GMA process was primarily focused on welding applications, and some fundamental research has been carried out. Ribeiro et al. [11–13] studied the arc behaviour and the metal transfer dynamics in the CW-GMA process and also compared with the standard GMA process. They found that the transition of metal transfer from a globular mode to a spray mode occurred at a slightly lower current in the CW-GMA process compared to that in the standard GMA process, and the arc resistance reduces with the increased cold wire feed speed (CWFS), resulting in an increase in arc current [11]. The increase of the CWFS in the CW-GMA process facilitates the arc attachment to the cold wire [12]. In addition, they found that the arc wandering issue in the standard pulsed GMA (P-GMA) process with pure argon shielding gas can be suppressed with the cold wire addition due to the migration of cathode spots to the cold wire, which increased the process stability and resulted in a good bead shape [13]. The cold wire with P-GMA process, referred to as CW-P-GMA, was also studied by Ribeiro et al. [14] and Jorge et al. [15] due to the lower energy input of it compared to that of the CW-GMA. In addition, Assunção et al. [16] and Ribeiro et al. [17] used the CW-GMA for narrow gap welding application and claimed that compared to the standard GMA process, the CW-GMA improved the productivity and reduced the arc wandering to the groove sidewalls due to the arc attachment to the cold wire. Furthermore, it was reported that the residual stress was reduced [18] and the fatigue performance was improved [19] with the CW-GMA process compared to that with the standard GMA process. Only a limited amount of research has been dedicated to the application of the CW-GMA process in AM. These studies primarily focused on investigating the combination of hot wire and cold wire for metallurgy [20] and conducting simple mechanical analysis [21].

Although many benefits were reported for CW-GMA welding process, it has not been examined for high productivity AM applications. In addition, the optimum processing conditions for welding and AM are different due to the different requirements for the two cases [22–24]. For example, high deposition rate is more desirable in AM compared to welding, as more material is normally deposited in the former case. However, the limit of the deposition rate in the CW-GMA process is unknown. In addition, a single bead is the building block for the printed components, and its geometry determines the surface quality and deposition strategy [25]. How the bead shape changes with the cold wire addition is unclear. Additionally, a model to predict the geometry of the multi-layer single-pass walls is needed for the selection of required process parameters to build different engineering structures. Furthermore, with the addition of cold wire, the microstructure and mechanical properties of the components built with the CW-GMA process are expected to be different from those with the standard GMA process due to the different energy profiles. In particular, with reduced remelting and reheating, improved microstructure and mechanical properties could be anticipated. Therefore, it is of vital significance to examine the performance of the CW-GMA process for AM application.

In this study, the limit of the deposition rates at different levels of energy input of the CW-GMA process was investigated. The effect of the cold wire addition on the bead geometry was examined. The working envelope and the process model of the CW-GMA process was obtained for multi-layer single-pass walls. Two single-pass wall structures were built with the standard GMA and CW-GMA processes to compare their microstructure and mechanical properties. Furthermore, a large-scale industrial-level component was built with the CW-GMA process to evaluate its feasibility for high deposition rate applications.

2. Experimental

2.1. Materials and setup

In this study, the wires fed through the GMA torch and the external wire feeder are referred to as hot wire and cold wire, respectively. The material used for both hot wire and cold wire was high strength low alloy steel (ER90S-G) with a diameter of 1.2 mm, and the composition of the wire is shown in Table 1. Deposition was performed on mild steel substrates with dimensions of 300 mm × 200 mm × 12.7 mm. Prior to deposition, the substrates were ground and cleaned with acetone to remove any surface contamination. The shielding gas used for the GMA torch was composed of 8% CO_2 and 92% Ar (BOC Specshield gas). The flowrate of the shielding gas was 18 l/min during deposition. Fig. 1 schematically shows the experimental setup for the CW-GMA based wire-arc DED process. An EWM (Alpha Q552) power source was used to provide the electric arc, which was integrated with a wire feeder (Phoenix Drive 4) to feed the hot wire. Another wire feeder (Technical Arc) was used to feed the external cold wire. An arc monitor (AMV 4000) was connected to the power source to record the arc current and voltage. A CMOS camera (Xiris XVC-1000) was placed to the side of the melt pool to monitor the metal transfer and melt pool behaviour. The substrate was fixed to a workbench by clamps and the motion of the torch was provided by a 6-axis ABB robot.

Fig. 2 shows the configuration of the cold wire, GMA torch, and substrate. The torch was placed perpendicular to the substrate and the cold wire was fed laterally with an angle of 25°. The contact tip to workpiece distance (CTWD) used was 16 mm. The two wire tips meet at the top surface of the substrate. During deposition, the substrate was fixed, whilst the GMA torch and cold wire were moved along the travel direction with a front feeding configuration (i.e., cold wire at the front of the GMA).

2.2. Methods

2.2.1. Deposition rate and bead geometry

Bead-on-plate (i.e., single-layer single-pass deposition) experiments were conducted to study the limit of deposition rate and the variation of bead geometry at different levels of energy input. As mentioned earlier, unlike non-consumable electrode arc processes where the arc current is independent from the material feeding rate, the arc current in the GMA process is coupled with the hot wire feed speed (HWFS). Therefore, prior to the experiment, the arc current and voltage as a function of HWFS were measured, as shown in Figs. 3a and 3b. The output power of the power source is a product of arc current and arc voltage, and this output power as a function of HWFS and arc current can then be obtained, as shown in Figs. 3c and 3d, respectively. One can see that the output power increases with an increase in both HWFS and arc current. It should be mentioned that, to achieve high deposition rates, spray transfer mode (high power) was used rather than short circuit mode (low power) and globular mode (intermediate power). Additionally, the spray mode of the GMA provides a relatively long and stable arc column compared to that with the other two modes [26], which gives enough

Table 1
Chemical composition (in wt%) of both the hot wire and cold wire.

C	Mn	Si	S	P	Cr	Mo	Ni	V	Cu	Nb	Fe
0.09	0.90	0.56	0.001	0.006	2.5	1.07	< 0.1	< 0.01	< 0.1	< 0.01	Balance

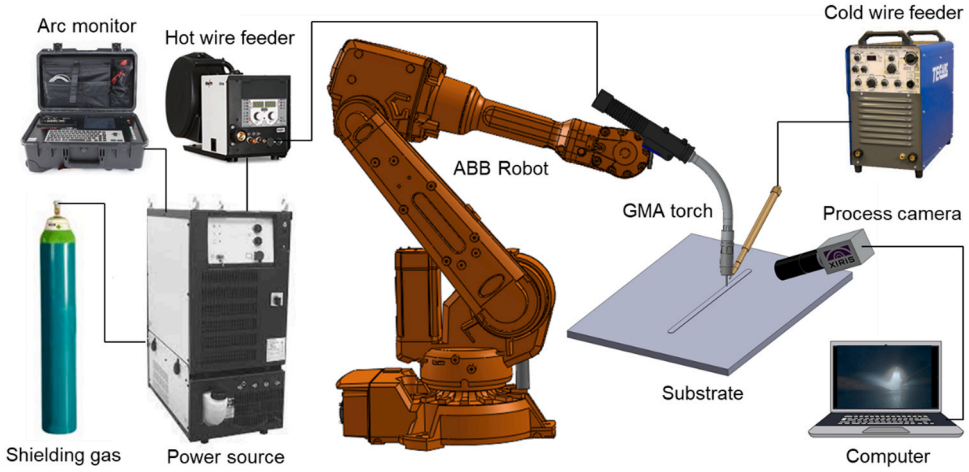

Fig. 1. Schematic showing the experimental setup for the CW-GMA based wire-arc DED system.

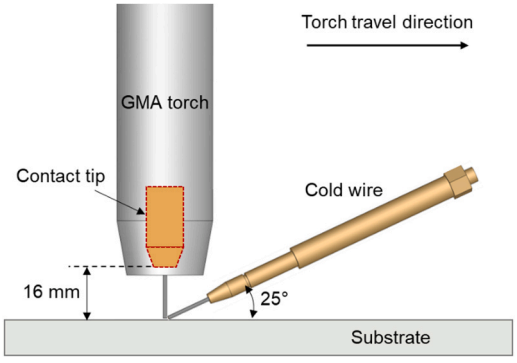

Fig. 2. Schematic showing the configuration of the GMA torch, cold wire, and substrate.

space to accommodate the cold wire.

The deposition rate is determined by how much wire can be fed and fully melted in the arc. In CW-GMA process, with the same hot wire and cold wire, the deposition rate, R, is expressed by:

$$R = \frac{\pi d^2 \rho (v_c + v_h)}{4} \quad (1)$$

where d is the wire diameter, ρ is the material density, v_c and v_h are CWFS and HWFS, respectively. One can see that for the CW-GMA process with the same hot wire and cold wire, the deposition rate is determined only by the total wire feed speed. In this study, the maximum deposition rates at four different levels of energy input were obtained, where the HWFS used was 6, 8, 10, and 12 m/min with the corresponding arc current of 233, 301, 363, and 404 A. In these experiments, for a certain energy input, the CWFS was increased from 0 to a limit value where the cold wire could not be fully melted as identified by the process camera. The travel speed (TS) was kept constant at 10 mm/s. After deposition, all the beads had a same length of 120 mm, and the bead dimensions were measured at the length of 40 mm, 60 mm, and 80 mm from the initiation, and an average value was used. The bead geometry is characterised by bead width and bead height (see Fig. 4a). In addition, the dilution, D, is given by:

$$D = \frac{A_2}{A_1 + A_2} \quad (2)$$

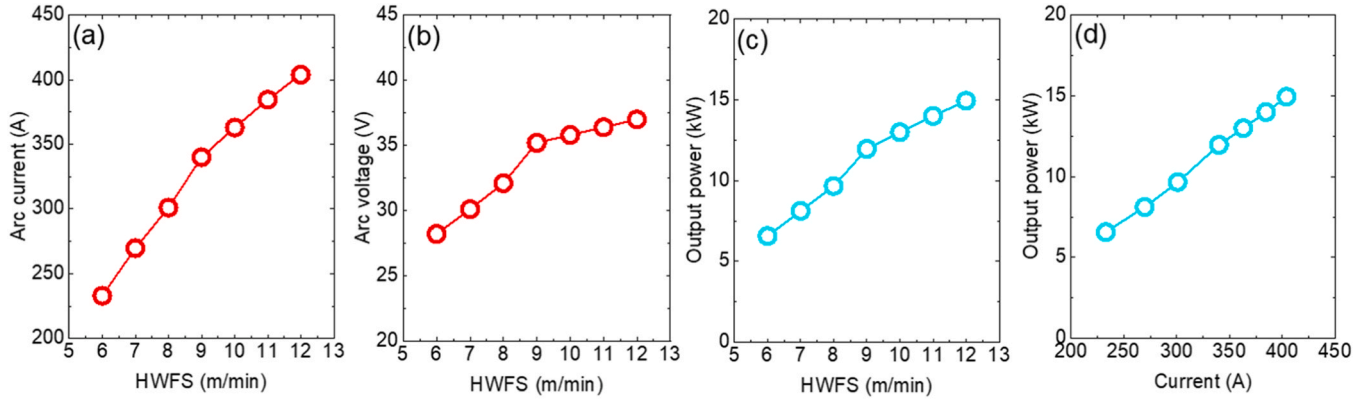

Fig. 3. Calibration of the power source: (a) arc current as a function of HWFS, (b) arc voltage as a function of HWFS, (c) output power as a function of HWFS, and (d) output power as a function of arc current.

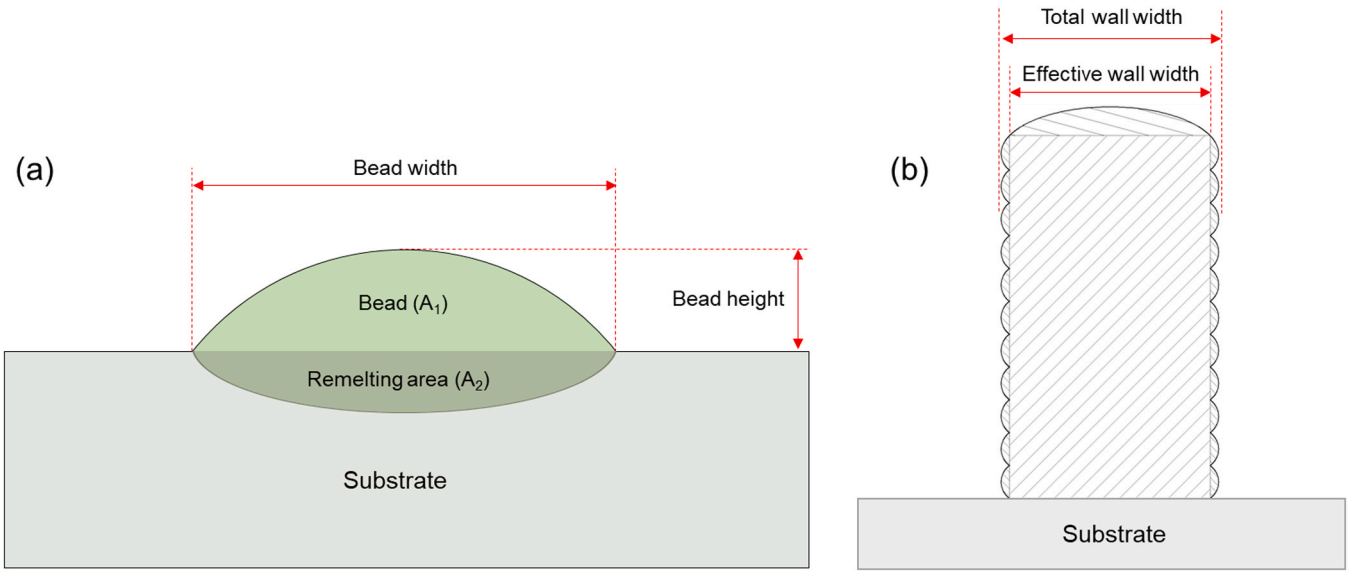

Fig. 4. Schematic diagrams showing: (a) the definition of the bead width, bead height, cross-sectional area of the bead (A_1), and the remelting area of the substrate (A_2); (b) the definition of the total wall width and effective wall width.

where A_1 is the cross-sectional area of the bead and A_2 is the remelting area of the substrate, as shown in Fig. 4a.

2.2.2. Working envelope and process model

The working envelope (or process window) of the CW-GMA process was obtained before achieving the geometric process model for multi-layer single-pass walls. Bead-on-plate experiments were first conducted, and the working envelope based on bead-on-plate was obtained in order to reduce the work to achieve the working envelope for multi-layer single-pass walls. In this process, two process parameters were kept constant, and the other was increased from a low value to a limit value. In total, 26 beads were deposited to understand the limitations of the process. With the same approach, 44 wall structures were then built to achieve the working envelope for multi-layer single-pass walls. When the working envelope of the process was achieved, D-optimal design of experiment (DoE) method was used to generate the process parameters for achieving the process model. More detailed introduction of the design method can be found in Ref. [27]. In this model, HWFS (m/min), CWFS (m/min), and TS (mm/s) were selected as the factors. As cubic behaviour was expected, three-factor third-order polynomial functions were fitted:

$$Y = \beta_0 + \sum_{i=1}^{3}\beta_i x_i + \sum_{i=1}^{3}\beta_{ii}x_i^2 + \sum_{i=1}^{3}\beta_{iii}x_i^3 + \sum_{i<j}^{3}\beta_{ij}x_i x_j + \sum_{i\neq j}^{3}\beta_{iij}x_i^2 x_j + \beta_{123}x_1x_2x_3 \quad (3)$$

where Y is the predicted response; β_0, β_i, β_{ii} and β_{iii} are the constant process effect, linear effect, quadratic effects and cubic effects of x_i, respectively; β_{ij}, β_{iij} and β_{123} are the interactions of first order, second order, and third order, respectively. The software (Design Expert) indicated that 28 sets of process parameters are necessary to calculate the regression coefficients for the full model. Therefore, 28 multi-layer single-pass walls were built, and each of them had 10 layers and a length of 120 mm. The interlayer temperature was controlled to be below 80 °C. The walls were built from alternative directions. After being finished, the walls were cross sectioned at the length of 40, 60, and 80 mm to measure the geometry. The three responses used in this model were effective wall width (EWW), layer height (LH) and surface waviness (SW). The definition of TWW and EWW is shown in Fig. 4b, and the surface waviness is defined by: $SW = (TWW - EWW)/2$.

2.2.3. Microstructure and mechanical properties

To examine the microstructure and mechanical properties of the components produced by the CW-GMA process, a multi-layer single-pass wall was built. In addition, another wall was built with the standard GMA process to compare with the wall built with the CW-GMA process. Both walls were deposited in an alternating direction manner to achieve an equal height at both ends. The process parameters used for the deposition of the two walls are shown in Table 2. It should be mentioned that a relatively high TS of 15 mm/s was used for the deposition of the two walls, which allows to achieve a thin geometry and low interlayer dwell time. During deposition, the interlayer temperature of the two walls were controlled below 80 °C. After deposition, both walls have the same length of 220 mm and height of 120 mm.

Tensile samples were extracted from the two walls both in vertical and horizontal orientations, as shown in Fig. 5a. According to BS EN 2002–1:2005 standard, the dimensions of the tensile samples are shown in Fig. 5b. Room temperature tensile test was conducted on an electro-mechanical testing machine (Instron 5500R) at a crosshead speed of 1 mm/min, and the tensile strain was recorded by a laser extensometer. Crystallographic orientation maps were obtained using a TESCAN S8000G field emission gun scanning electron microscope (SEM) equipped with an Oxford Instruments' Symmetry electron backscattered diffraction (EBSD) detector with an accelerating voltage of 15 kV, a beam current of 6.5 nA and a step size of 0.7 μm. Prior austenite grains (PAG) were reconstructed using the Nishiyama-Wasserman orientation relationship after filling in non-indexed pixels.

2.2.4. Evaluation of the process with component building

To evaluate the feasibility of using CW-GMA process to build

Table 2
Process parameters used for deposition of the two single-pass multi-layer walls.

Parameters	Wall 1 (CW-GMA process)	Wall 2 (standard GMA process)
HWFS (m/min)	9	9
CWFS (m/min)	8	0
TS (mm/s)	15	15
Interlayer dwell time (min.)	7	10
Total layer number	51	92
Average layer thickness (mm)	2.35	1.30

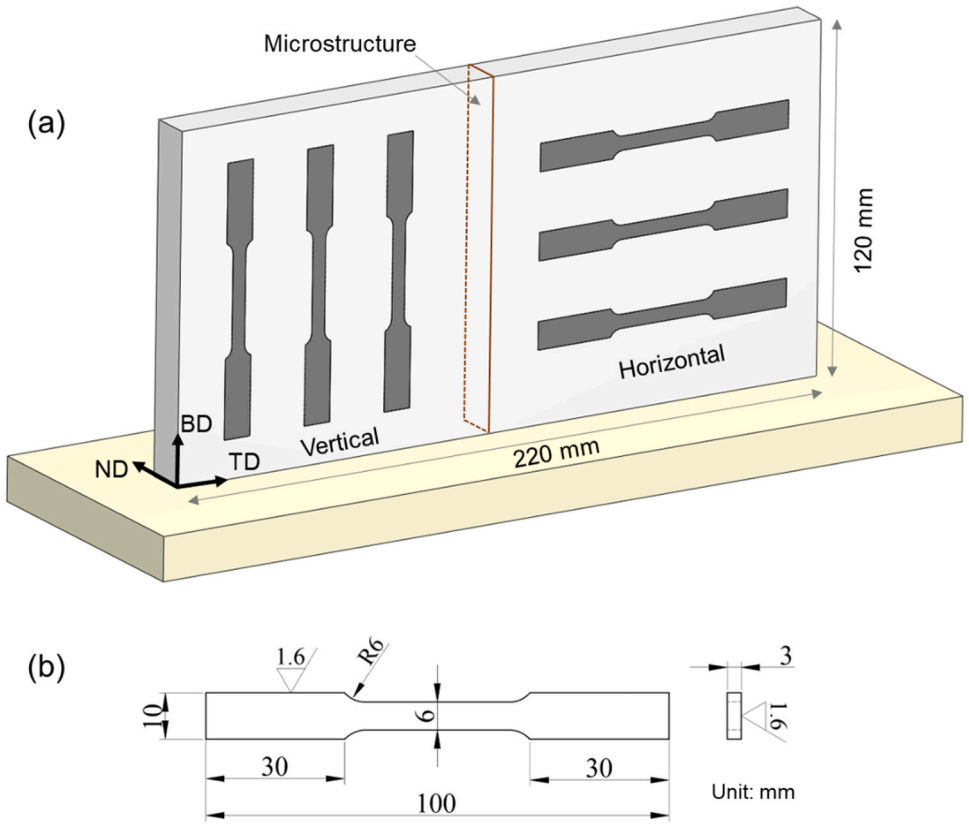

Fig. 5. Schematic showing (a) the location of the samples extracted from the two walls for tensile test and microstructure analysis, and (b) the dimensions of the samples for tensile test. Note, BD - building direction, TD - transverse direction, ND - normal direction.

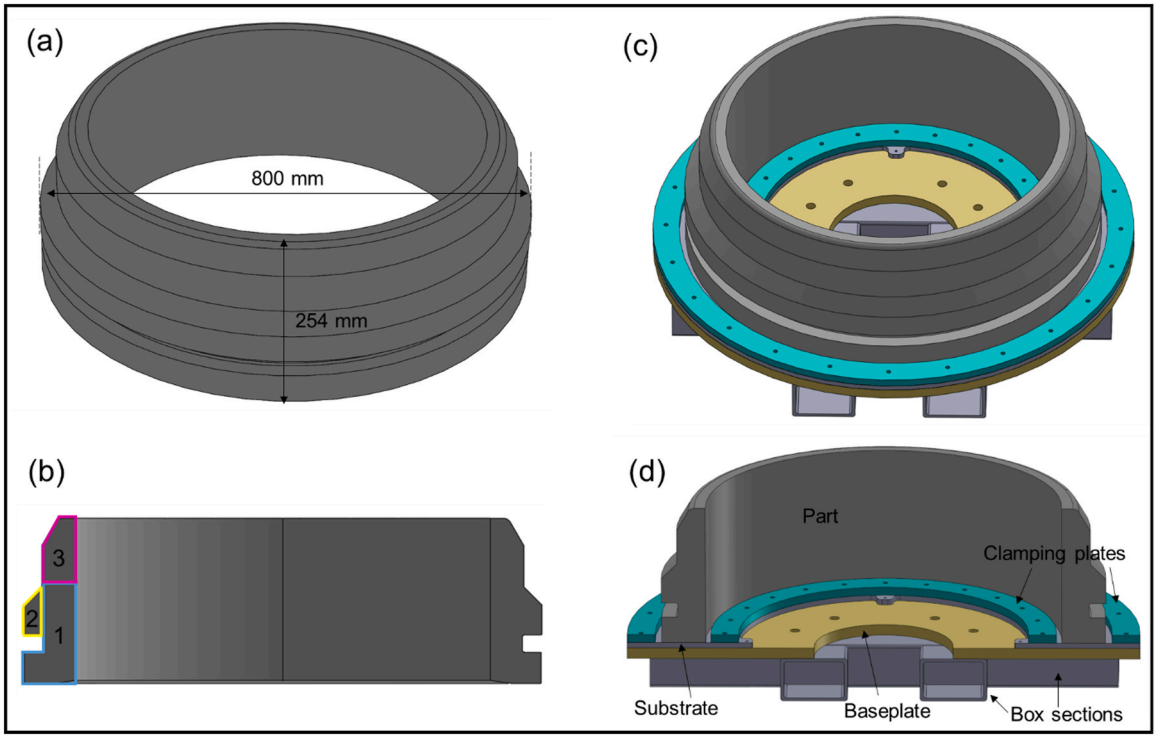

Fig. 6. (a) The geometry of the component, (b) the cross-section and deposition sequence of the component, (c) the component and the tooling design for the deposition, and (d) the cross-section of the component and tooling design.

industrial-scale components, an engineering structure with a weight of 280 kg was deposited. Fig. 6a shows the geometry of the component, and Fig. 6b shows the cross-section of the component, which has a maximum diameter of 0.8 m and height of 0.254 m. The same hot wire, cold wire and shielding gas that described in Section 2.1 was used for building this component. In addition to the shielding gas from the GMA torch, a local shielding device was attached to the torch to provide additional shielding for the material [28]. Pure argon with a flowrate of 80 l/min was used for the local shielding device. Since the process stability largely depends on the cold wire position, a motorised stage was used to control the cold wire position during the deposition process. Due to the high energy input introduced to the substrate, a customised tooling and jig was designed to restrict the distortion of the substrate, as shown in Figs. 6c and 6d. The substrate has a thickness of 10 mm, whilst a 20 mm thick baseplate was placed underneath to hold the substrate. To increase the strength of the baseplate, some box section steels were welded underneath to support the baseplate. In addition, two clamping plates were used to fix the substrate. As the tooling design is not the focus of this section, more detailed information will not be introduced here.

Since the component has a rotating geometry, a turntable was used to build the component and thus to reduce the rotation of the torch and cold wire. During the deposition process, the GMA torch was stationary whilst the turntable was rotating to provide the motion for material deposition. A coordinated motion between the robot and turntable was used to ensure that the required travel speeds are achieved automatically when the torch is at different positions with respect to the turntable. As shown in Fig. 6b, there are three steps for the component building. Section 1 was first built layer by layer. Due to the overhang of section 2, the turntable was flipped by 90° when section 1 was completed, and then section 2 was deposited on the side surface of section 1. When section 2 was finished, the turntable was flipped back, and section 3 was deposited on the top of section 1 until the completion of the component. Parallel deposition strategy was used for the component building, where concentric beads were deposited next to each other in each layer. Due to the large melt pool formed in the CW-GMA process, a skin & core strategy was adapted to achieve good surface finish of the component [29]. That is, the outer contour of the component was deposited with a smaller bead geometry at a relatively low deposition rate, whilst the inner core section was deposited with a larger bead geometry at a high deposition rate. The parameters used for the skin and core passes are shown in Table 3. During deposition, the bead shape is not uniform at the start and end (taller and narrower at the start, while shallower and wider at the end) due to the unstable thermal conditions. Therefore, for each layer, the deposition starts from different positions to reduce the accumulation of the nonuniform geometry and thus avoid any associated defects.

3. Results and discussion

3.1. Deposition rate and bead geometry

3.1.1. Deposition rate

Fig. 7 shows the deposition process at the same energy input but with two different cold wire feeding rates. As shown in Fig. 7a, at a CWFS of 10 m/min, the cold wire was fully melted, which led to a stable process and a smooth bead surface (see Fig. 7c). However, when the CWFS was increased to 12 m/min, the energy from the GMA could not fully melt the cold wire, and the unmelted wire came out from the back of the melt pool, as indicated by the yellow arrow in Fig. 7b. The resultant bead in this case was shown in Fig. 7d, where the unmelted wire still can be seen when the material was solidified. In the second case, numerous spatters were generated due to the interception of the GMA by the cold wire. In addition, the melt pool was stabbed by the cold wire in this case, causing a violent melt pool and therefore an unstable deposition process. Based on the observation and analysis from the deposition process recorded by the process camera, the maximum CWFS under this energy input was 10 m/min.

Table 3
Process parameters used for the skin and core passes for building the component.

Parameters (unit)	Skin passes	Core passes
HWFS (m/min)	8	11
CWFS (m/min)	4	8
TS (mm/s)	10	10

The same experiments were repeated for different levels of energy input. Figs. 8a and 8b show the maximum CWFSs and deposition rates achieved with different HWFSs (i.e., energy inputs), respectively. In Fig. 8a, the maximum CWFS achieved increases with an increase in the HWFS. This is easy to understand that more material can be melted at a higher energy input. Based on Fig. 8a and Eq. (1), the maximum deposition rate achieved as a function of HWFS is shown in Fig. 8b. The maximum deposition rate achieved in this study was 14 kg/h at a HWFS of 12 m/min and CWFS of 14 m/min.

To compare the deposition rate of the CW-GMA process with a non-consumable electrode based process, the maximum deposition rate for the PTA process was examined at an arc current of 233 A. A maximum wire feed speed of 4.5 m/min was obtained at this arc current for the PTA process. Fig. 8c shows the deposition rates achieved with the CW-GMA, standard GMA and PTA processes at different levels of arc current. Compared to the standard GMA process, the deposition rate in the CW-GMA process was improved significantly at all levels of arc current examined. The PTA process has the lowest deposition rate among the three processes although only one arc current condition was examined. It also can be seen from Fig. 8c that the maximum deposition rates at different levels of arc current increased by more than double when cold wire was added, which is reflected in Fig. 8a where the ratio of the maximum CWFSs to the corresponding HWFSs are slightly higher than 1. In addition, it is reported that another non-consumable electrode based process, GTA, has slightly lower deposition rates than the PTA process due to the less constricted arc column and lower energy density presented [5]. This means that with a single power source, the CW-GMA process has the highest deposition rate among all the wire-arc DED processes provided that the same energy input is applied.

In AM, the deposition process efficiency can be reflected by the energy consumed for deposition per unit mass of material [30]. Higher deposition process efficiency means that less energy is needed to deposit a certain amount of material. In this study, at an arc current of 233 A, the same arc voltage of 28 V was observed for the three processes examined, giving a power input of 6.5 kW for each process. From Fig. 8c, at the arc current of 233 A, the maximum deposition rates obtained with the CW-GMA, standard GMA and PTA processes were 6.4, 3.2 and 2.4 kg/h, respectively. This gives 3.7, 7.3 and 9.8 MJ/kg of the energy needed for per unit mass of material for the three processes, respectively. This means that to build a same component, much less energy is needed with the CW-GMA process compared to other wire-arc DED processes (here, 50% and 62% energy reduction compared to that in the standard GMA and PTA processes, respectively).

3.1.2. Bead geometry

Compared to the standard GMA process, the addition of the cold wire in the CW-GMA process not only increases the deposition rate, but also leads to changes in the bead shape and remelting. Fig. 9 shows the effect of CWFS on bead shape at different levels of arc current. As shown in Fig. 9a, for a given current, the bead width increases first and then reaches a plateau (or reduces slightly). The increased bead width was attributed to the increased melting efficiency, as more energy was used for wire melting rather than loss from the substrate. However, when the CWFS was increased to a certain level, the cold wire could not be fully melted only by the arc. Instead, it reaches the melt pool and takes a large amount of energy from it, which impedes the spread of the melt pool in

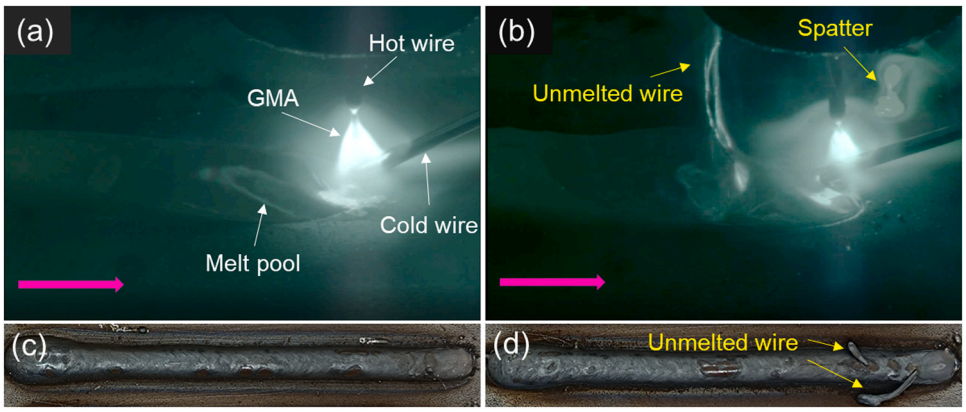

Fig. 7. A comparison of the process stability and bead appearance achieved with the same HWFS of 8 m/min but different CWFSs: (a) the deposition process at a CWFS of 10 m/min, (b) the deposition process at a CWFS of 12 m/min, (c) bead appearance at a CWFS of 10 m/min, and (d) bead appearance at a CWFS of 12 m/min. Pink arrows indicate the torch travel direction.

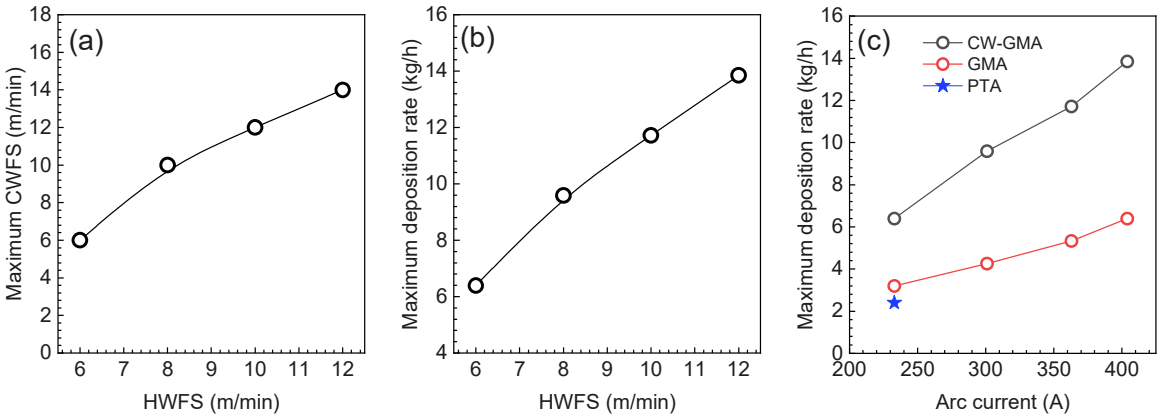

Fig. 8. (a) The maximum CWFS and (b) the maximum deposition rate achieved as a function of HWFS; (c) The maximum deposition rates achieved for steel with different wire-arc DED processes at a wide range of arc current.

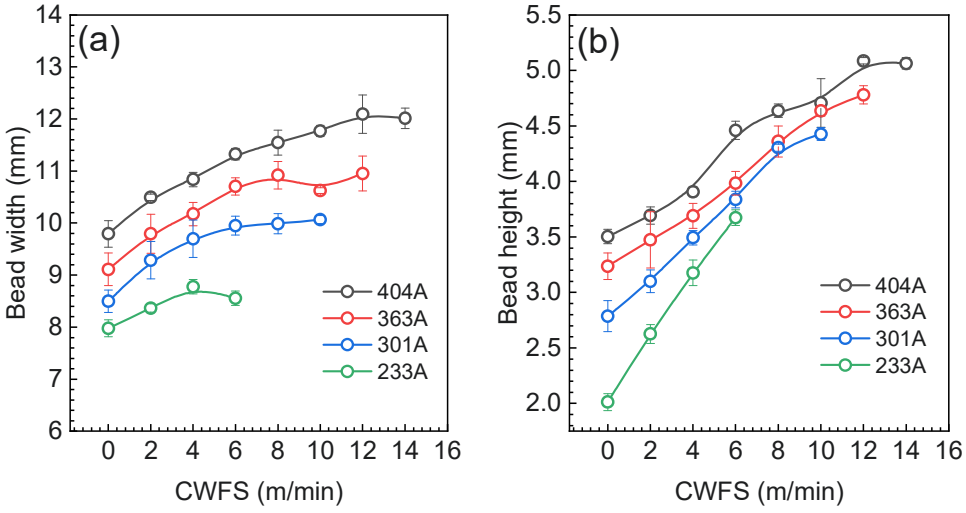

Fig. 9. The effect of CWFS on the bead shape at different levels of arc current: (a) bead width, and (b) bead height.

the width direction. Similar phenomenon was observed in the PTA based process [9]. It also can be seen that for a given CWFS, the bead width increases constantly with an increase in the arc current, which is not only because of the increased energy input but also because of the increased amount of material deposited. As for the bead height, it increases constantly with both CWFS and arc current due to the increase in material feeding rate (Fig. 9b).

Fig. 10a shows the cross-section of the beads as a function of CWFS in some cases described in Fig. 9, and Figs. 10b and 10c show the dilution and the total melted area (including bead and substrate) in these cases. It

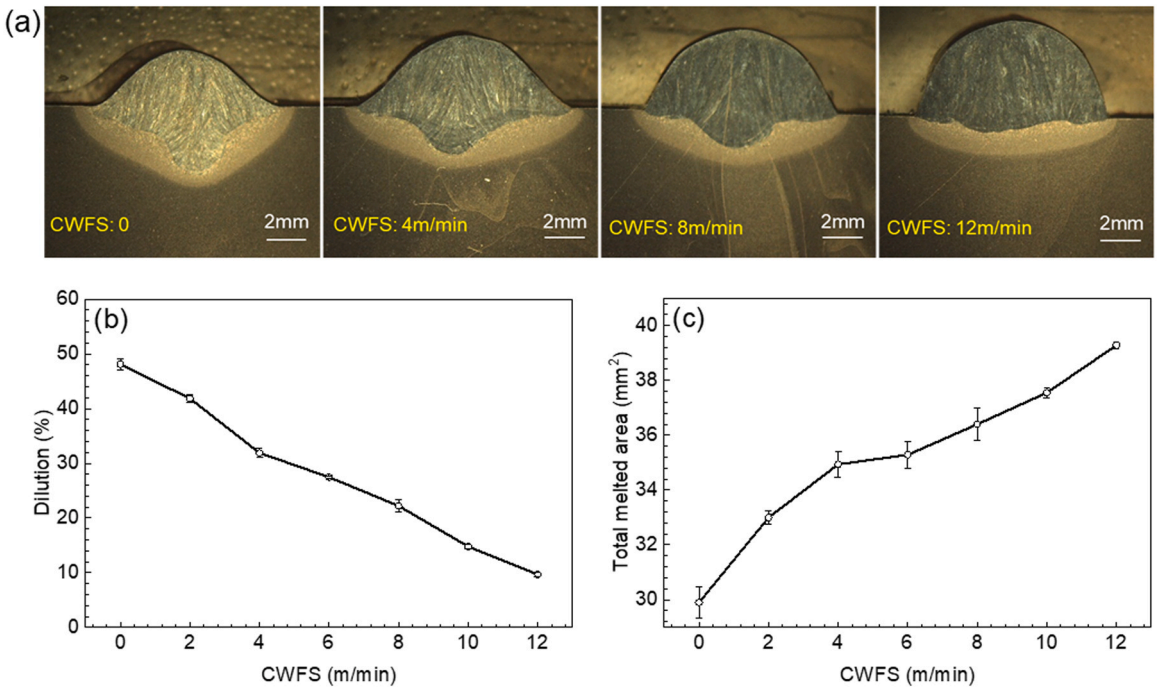

Fig. 10. (a) Cross-section of the beads obtained with different CWFSs at the same arc current of 301 A, (b) the dilution, and (c) the total melted area of the corresponding beads.

can clearly be seen from Fig. 10a that the remelting area reduces significantly as the CWFS increases from 0 to 12 m/min. Without the addition of the cold wire, a high dilution of 48% was observed, meaning that almost half of the energy used for generating the fusion zone was consumed in melting the already-existed material (Fig. 10b). However, the dilution was reduced significantly to below 10% at a CWFS of 12 m/min. Fig. 10c shows that the total melted area increases constantly with an increase in the CWFS. This is because, as mentioned earlier, the thermal loss from the cold wire to its surroundings is much less than that from the substrate, and therefore more energy was used in melting the wire and less in melting the substrate.

In fact, the melted area represents the melting efficiency of the process. The melting efficiency, η_m, is defined by the energy used for generating the fusion zone divided by the net energy transferred to the workpiece, which is expressed as [12]:

$$\eta_m = \frac{(A_1H_1 + A_2H_2)v}{\eta_a VI} \tag{4}$$

where A_1 and A_2 are the cross-sectional area of the bead and the melted area of the substrate, respectively; v is the TS, η_a is the arc efficiency, V is the arc voltage, and I is the arc current; H_1 and H_2 are the volumetric enthalpy (in J/mm^3) of the bead and substrate, respectively, which can be calculated from Eq. (5).

$$H = \frac{T_m^2}{300000} \tag{5}$$

where T_m is the melting point of the material. Based on Eqs. (4) and (5) and the melted area measured in the first case and the last case in Fig. 10a, the melting efficiency for the cases without the cold wire and with a CWFS of 12 m/min are 40.6% and 53.4%, respectively. This means that the melting efficiency was increased with the addition of cold wire, indicating that more energy was used for melting the material rather than dissipated to the surroundings.

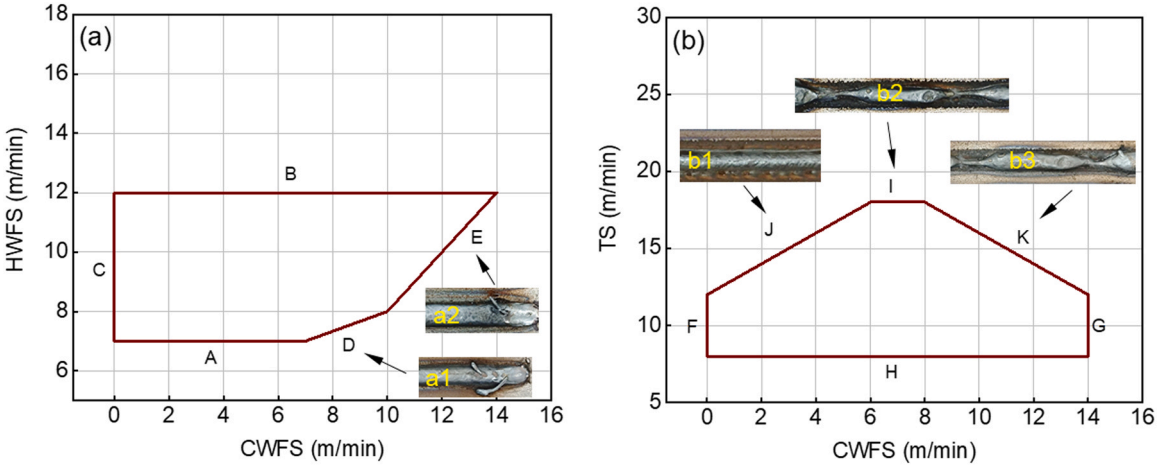

Fig. 11. Working envelope of the CW-GMA process based on bead-on-plate experiments: (a) HWSF vs CWFS, and (b) TS vs CWSF.

3.2. Process model

3.2.1. Working envelope

Fig. 11 shows the working envelope of the CW-GMA process based on bead-on-plate experiments. The boundaries of the working envelope are limited by different conditions, such as deposition rate, the occurrence of defects, and hardware. It should be mentioned that all the three parameters (HWFS, CWFS, and TS) used should be within the working envelope indicated in Figs. 11a and 11b simultaneously. In this envelope, the bottom boundary of HWFS (A) represents the threshold between globular and spray transfer modes, where spray mode is preferred in this process due to the high process stability and high deposition rate required. The top boundary of the HWFS (B) is limited by the rating of the torch. The boundaries of CWFS (D, E, G) are determined by the maximum amount of cold wire that can be melted, which can be obtained from Fig. 8a. Images a1 and a2 show two examples of the incompletely melted wires. The bottom boundary of TS (H) is due to the need for high productivity, and therefore lower values are not considered here. The top boundaries of the TS (I) and boundary (K) are due to the presence of humping, as shown in images b2 and b3. Boundary (J) is due to the occurrence of undercut, as shown in image b1. For the single-layer deposition with the CW-GMA, defect-free beads can be achieved when the selected process parameters are within this working envelope.

Fig. 12 shows the working envelope of the CW-GMA process for multi-layer single-pass walls (the blue solid lines). One can see that the working envelope for multi-layer deposition is smaller compared to that for single-layer deposition (the brown dashed lines). This is because the boundary conditions for the two scenarios are quite different. In single-layer deposition, there is much material (i.e., substrate) to support the melt pool, and defects like overflow will not occur. However, in multi-layer condition, there is not much supporting material around the melt pool, the likelihood of overflow formation will be increased and the limits for the presence of other defects will also be different. In this working envelope, same as those in single-layer deposition, the bottom boundary (A) and the top boundary (B) of the HWFS are limited by the spray transfer mode and torch rating, respectively. Boundary (C) is due to the need for high deposition rate. Here, a minimum CWFS to HWFS ratio of 0.5 was used. Boundaries (D, E, F, L, M) are due to the presence of overflow, as shown in images a1, a2, a3, b1, b4. Boundaries (J, K) are limited by the presence of humping, as shown in images b2 and b3.

From the working envelope, two of the most observed defects in the CW-GMA process are humping and material overflow. Humping occurred at high TSs, as can be seen in Figs. 11b and 12b. It is also a commonly observed defect in other fusion welding processes, and the mechanism of its formation was revealed in Refs. [31–33]. Overflow is a common defect that occurs during multi-layer single-pass deposition in the standard GMA process due to the large melt pool created by the high energy input [3,34]. It is easier to occur in single-pass multi-layer deposition compared to that in multi-pass multi-layer deposition due to the less supporting material around the melt pool in the former case [34]. In the CW-GMA process, overflow cases were observed at high CWFSs. This is attributed to the large melt pool generated in these cases. Although the remelting is reduced with the increase in the CWFS, the melt pool is becoming larger due to the increased melting efficiency, as explained in Section 3.1.2. Consequently, the larger melt pool increased the risk of generating material overflow. In fact, the working envelope can be expanded by reducing the likelihood of defects occurring, which can be achieved by optimising the processing conditions applied. For example, use of some specific reactive shielding gases can suppress the occurrence of humping and allows up to 400% higher TS than use of pure argon shielding gas [32]. The working envelope shown in Fig. 12 provides guidance for process parameters selection to achieve sound single-pass wall structures in the CW-GMA process.

3.2.2. Process model

Fig. 13 shows the process model for predicting the geometry of multi-layer single-pass walls produced by the CW-GMA process. In Fig. 13a, the EWW is directly proportional to the HWFS and inversely proportional to the TS. However, it reduces with the increase in the CWFS. This is because relatively high CWFSs were used in the model (a minimum CWFS to HWFS ratio of 0.5) as mentioned in Section 3.2.1, and the bead width reaches a plateau or even slightly reduces with the increase in the CWFS, as can be seen in Fig. 9a. For the LH, the HWFS has a very little effect on it (Fig. 13b). This is because, on one hand, higher HWFS brings more material which should increase the height. However, on the other hand, the higher energy input will increase the spread of the melt pool in the width direction, which reduces the layer height. As a result, it does not change significantly with the increase in the HWFS. As with the EWW, the LH reduces with the increase in the TS due to the reduced material deposition per unit length. The CWFS has the most significant effect on the LH, with higher values causing larger layer height. In Fig. 13c, the process model for predicting the SW is relatively complex. This is mainly due to the formation of a large melt pool in the CW-GMA process, which resulted in a wide range of SW ranging from 0.77 to 2.77 mm. This range is higher than what was obtained with the PTA process as reported in Ref. [27]. Overall, there is a trade-off between the deposition rate and the resolution (or surface roughness) of the deposited components. Therefore, the skin & core deposition strategy is necessary when manufacturing components with the CW-GMA process to achieve both high surface finish and high deposition rate. Overall, the process model obtained shows how process parameters determine the geometry of single-pass wall structures, which can guide the selection of

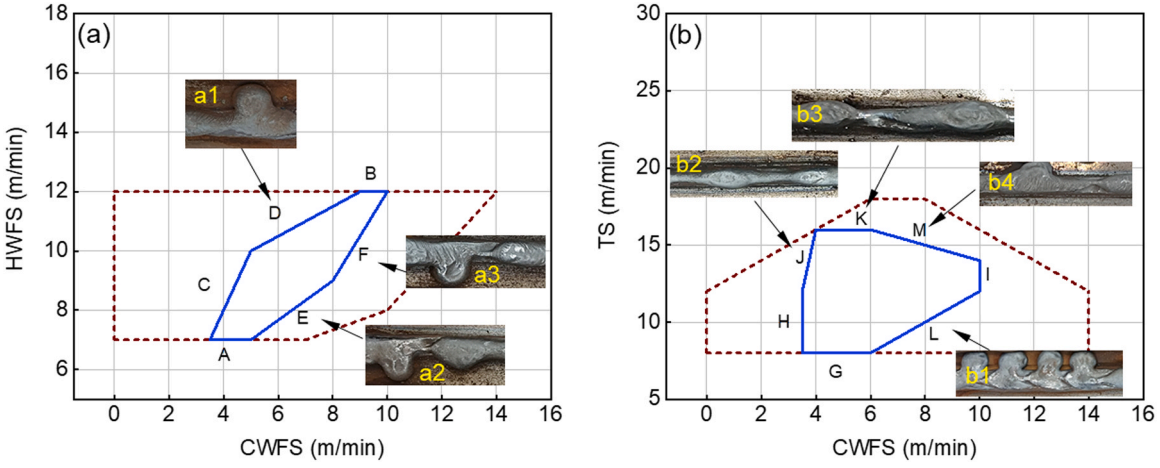

Fig. 12. Working envelope of the CW-GMA process based on multi-layer single-pass walls: (a) HWSF vs CWFS, and (b) TS vs CWSF.

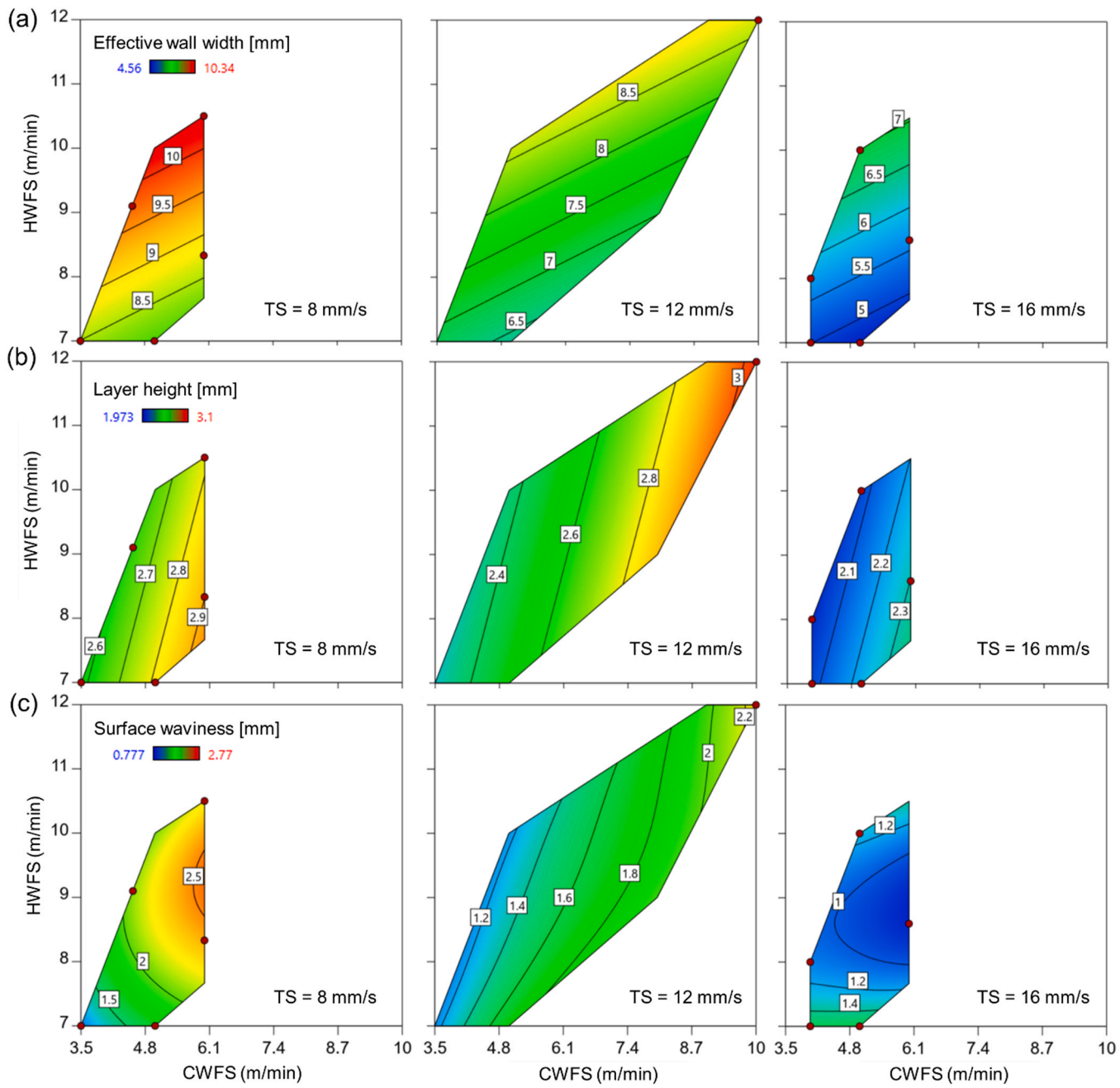

Fig. 13. Geometric process model for multi-layer single-pass walls of the CW-GMA based wire-arc DED: (a) effective wall width, (b) layer height, and (c) surface waviness.

appropriate parameters to achieve the desired geometry and deposition rate.

3.3. Microstructure and mechanical properties

Fig. 14 shows the tensile properties of the samples produced by both the standard GMA and CW-GMA processes. Four typical stress-strain curves are shown in Fig. 14a, including the samples in both orientations from the two processes. It can be observed that, compared to the samples produced by the standard GMA process, the samples produced by the CW-GMA process have higher strength and slightly lower elongation. The detailed values of the tensile properties are shown in Fig. 14b. The yield strength of the samples produced by the CW-GMA process was increased by 17 MPa and 65 MPa in the horizontal and vertical orientations, respectively, compared to the samples produced by the standard GMA process. The ultimate tensile strength was increased by 47 MPa and 83 MPa in the two orientations, respectively. This compromises the elongation by a slight reduction of 3.6% and 2.3% in the two orientations, respectively. In addition, the anisotropy of the tensile properties was reduced which can be seen from the yield strength (the difference in the two orientations reduced from 37 to 11 MPa) and elongation (reduced from 1.5% to 0.2%), although no significant improvement was found in the ultimate tensile strength. As the mechanical properties are highly dependent on microstructure evolution, an in-depth analysis of the microstructures obtained with the two processes were conducted.

Ferrite and reconstructed austenite phase EBSD maps of the GMA and CW-GMA samples are compared in Fig. 15(a1-a2) and Fig. 15(b1-b2), respectively, highlighted in inverse pole figure (IPF) colouring relative to the BD. From the ferrite EBSD maps (Fig. 15 (a1, b1)), fine

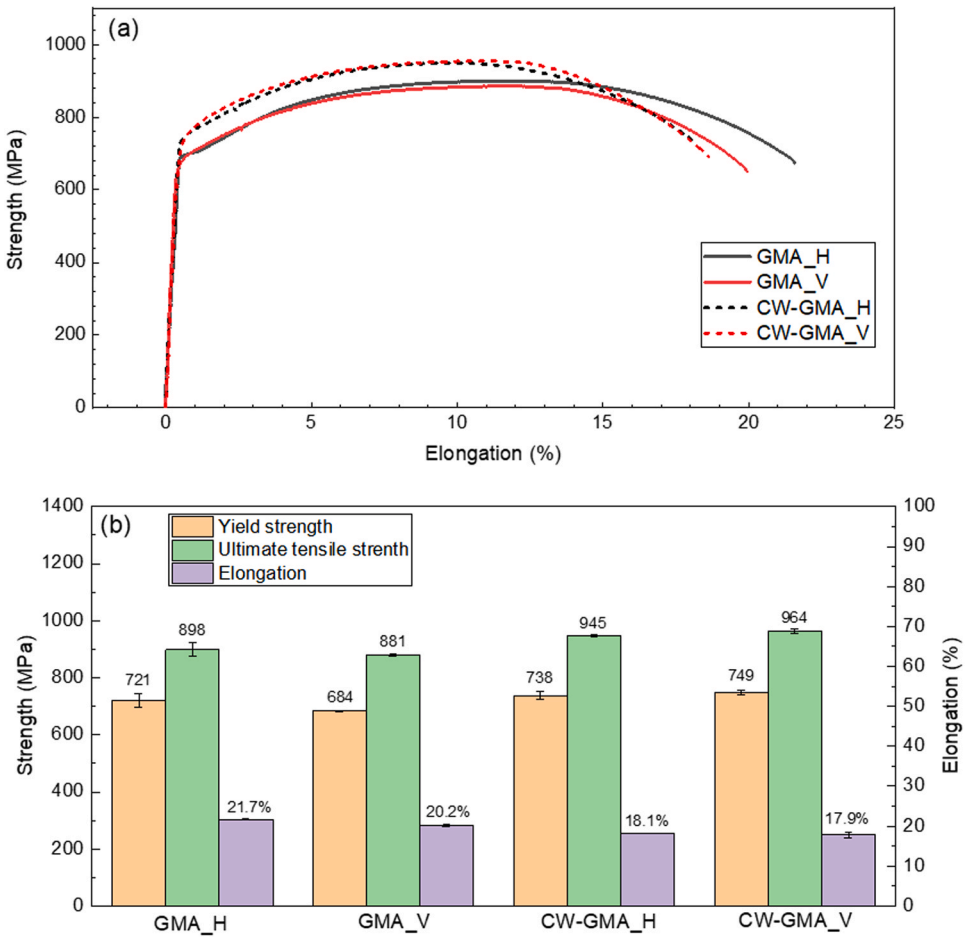

Fig. 14. Tensile property of the samples produced by standard GMA and the CW-GMA processes: (a) four typical stress-strain curves with two different orientations by the two processes, and (b) the mean values of the strength and elongation in each condition. Note, GMA_H and GMA_V represent the samples in horizontal and vertical orientations produced by the standard GMA process, respectively, whilst CW-GMA_H and CW-GMA_V represent the samples in horizontal and vertical orientations produced by the CW-GMA process, respectively.

lath-like ferritic microstructure in random crystallographic orientation can be observed throughout the samples, combining in the blocky form with apparent directionality. By reconstruction following the Nishiyama–Wassermann (N-W) orientation relationship (OR) of $\{111\}_{\gamma}//\{1\bar{1}0\}_{\alpha'}$ $\langle\bar{1}01\rangle_{\gamma}//\langle001\rangle_{\alpha'}$, distinct differences can be seen in prior austenite grain (PAG) structures between the GMA and CW-GMA samples (Fig. 15(a2, b2)). In comparison, the GMA sample exhibits a coarser columnar PAG structure than that of the CW-GMA sample across the central region, with a strong $\{110\}<110>$ rotate Goss and γ fibre texture along BD (indicated by the corresponding inverse pole figure and pole figure shown in Fig. 15(a3, a4)). Clearly, more fine equiaxed PAGs can be seen in the CW-GMA sample and the columnar PAGs are not overgrown in general. The PAGs orientation is also more random and diffuse in the CW-GMA deposit, leading to a considerable decrease in texture intensity and a tendency to be isotropic, as can be seen in Fig. 15 (b3, b4). The comparison on PAG size and aspect ratio distribution between GMA and CW-GMA samples is shown in Fig. 15(c, d). The average PAG size in the CW-GMA deposit is 126 μm, which is refined to one-third of that in the GMA counterpart. In the meantime, the grain aspect ratio of the CW-GMA sample is decreased due to the increased proportion of equiaxed PAGs. To discuss the consistency of the microstructure and properties of the single-pass multi-layer walls along the building direction, a supplementary material including 3 figures (Figs. S1-S3) was uploaded.

The size and morphology of the as-solidified PAGs are highly dependent on the thermodynamic and metallurgical status of the local melt pool in wire-arc DED [35]. During deposition, partial arc energy absorbed is responsible for melting the wire feedstock and deposit surface and the remaining is depleted by rapid thermal conduction into the deposit and surroundings [1]. In both the standard GMA and CW-GMA processes, when the energy input and TS were kept unchanged, the metallurgical thermodynamic and kinetic of the melt pool are governed by the specific energy density, which is defined by the energy used for melting per unit volume of wire. For the two walls built, the specific energy density for the standard GMA and CW-GMA processes was 56.4 GJ/m^3 and 29.9 GJ/m^3, respectively. Apparently, compared to the standard GMA process, the addition of the cold wire in the CW-GMA process significantly reduced the specific energy density and therefore led to a lower superheating degree of the melt pool. The equiaxed PAGs are either the products of recrystallisation when the reheating temperature exceeds Ac1 or newly nucleated within the melt pool. The residual or partially melted solid feedstock in the melt pool would be perfect heterogeneous nucleation sites for fine equiaxed PAGs during solidification and fewer reheating cycles achieved in the CW-GMA process no longer allow fine equiaxed PAGs to develop into columnar ones, leading to the mixed PAG structure. On the contrary, a higher energy input achieved by the standard GMA process led to a larger remelting depth and a steeper temperature gradient within the melt pool, making the epitaxial growth from the parent PAGs at the bottom of the pool overwhelm more favourable for the formation of columnar grains [36]. In addition, the size of PAGs in this case is also influenced by the cooling rate. Benefitting from a higher cooling rate in the CW-GMA process, the PAGs are not allowed to grow up excessively due to shorter growth duration, but this is not the case with PAGs in the GMA sample. It is known that coarse columnar grains are always associated with anisotropic mechanical properties and detrimental for applications involving multidirectional stresses while fine equiaxed grains result in uniform mechanical properties and help reduce solidification cracking suspicions [37]. This explains the anisotropy reduction of the tensile properties in

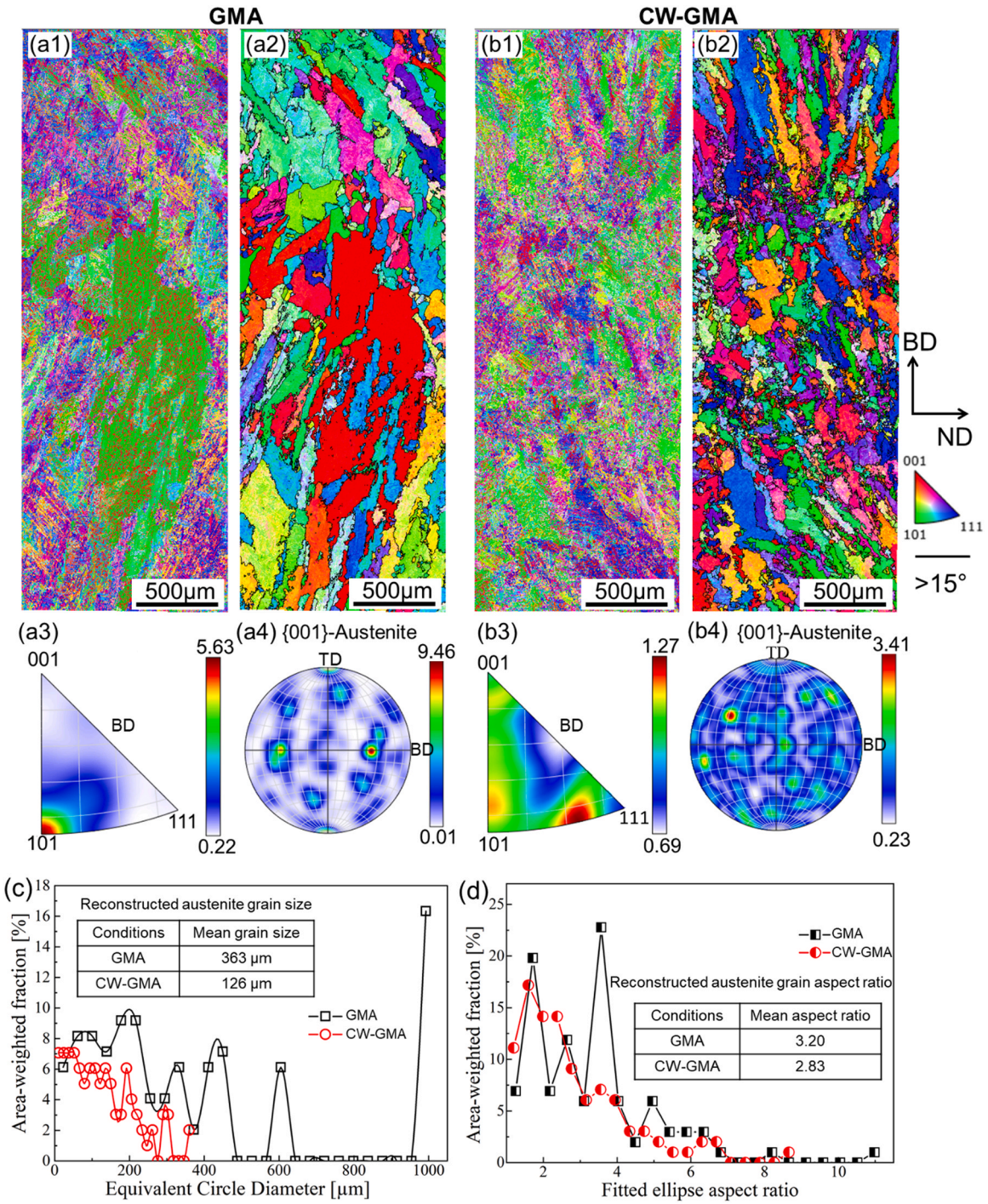

Fig. 15. EBSD inverse pole figure orientation maps for child-ferrite and reconstructed prior austenite, inverse pole figure and pole figure for reconstructed austenite phase taken from the BD-ND plane of (a1-a4) GMA-processed sample and (b1-b4) CW-GMA-processed sample; comparisons on (c) reconstructed austenite grain size distribution and (d) aspect ratio between GMA and CW-GMA processed samples.

the CW-GMA sample, possessing a mixture of equiaxed and columnar PAG structures. To sum up, with other deposition parameters kept constant, the size and morphology of PAGs are highly dependent on the specific energy density, which can be tailored by controlling the CWFS to HWFS ratio in the CW-GMA process.

3.4. Process evaluation with component building

Before depositing the component, the selection of process parameters was guided by the process window and process model. The process parameters should be selected within the process window to achieve defect-free beads. In addition, to achieve the desired bead geometry and deposition rate, the process model is needed. During the deposition of the component, due to the different parameters used for skin and core passes, the bead geometries for them are different. More specifically, the beads for skin passes are narrower and shallower than those for core passes. Therefore, the offset between the skin and core passes is smaller than that between core passes to avoid any lack of fusion. In addition, depending on the ratio of the skin height to core height, more skin layers are needed to ensure that the skin is always higher than core and thus to

restrict the large melt pool of core.

During the deposition of the component, the process had high stability in terms of the arc behaviour and metal transfer, as can be seen from the attached video [Video], where a HWFS of 11 m/min and a CWFS of 8 m/min were used for core pass deposition. It was found that the process is sensitive to the cold wire position. If the cold wire position is too high, it will intercept the material stream of the hot wire, resulting in a large number of spatters and reduced stability of the arc column. Conversely, if the cold wire position is too low, the contact area between the cold wire and the GMA is reduced, which will limit the deposition rate due to the less energy absorption by the cold wire. By using the spray mode and controlling the cold wire in an optimum position, the process was stable with very few spatters generated, and the beads were uniform in the whole process.

Supplementary material related to this article can be found online at doi:10.1016/j.addma.2023.103681.

Fig. 16 shows the deposition process of the component. Fig. 16(a-c) shows the deposition of the first layer of the component. One can see that the skin passes of the first layer were deposited first (Fig. 16a), and the core passes were then deposited (Figs. 16b and 16c). In total, 2 skin passes and 11 cores passes were deposited in the first layer. Fig. 16d shows the completion of section 1. Fig. 16e shows the deposition of section 2 of the component, which is on the side surface of section 1. Fig. 16f shows the final appearance of the component. One can see that the component exhibited good surface finish at a high deposition rate close to 10 kg/h. The total deposition time (i.e., arc on time) was around 30 h. This means that very little material is wasted after post machining, and the lead-time is very short compared to that built by the traditional manufacturing method. This demonstrated the high feasibility and advantages of using the CW-GMA process to build large-scale engineering structures.

In summary, this CW-GMA process is highly suitable for high deposition rate applications. Compared to the standard GMA process, three main benefits can be achieved with this process due to the addition of the cold wire. First, a high deposition rate can be obtained owing to the extra material input from the cold wire but with the same energy input, leading to high productivity. Second, the energy input and material input can be decoupled in this process, which enables to reduce the high remelting and reheating commonly seen in the standard GMA process. Third, due to the low energy input for melting per unit volume of material, both the grain size and anisotropy can be reduced, resulting in improved mechanical performance.

4. Conclusions

1. A maximum deposition rate of 14 kg/h was achieved with the CW-GMA based DED, which is the highest among all the wire-arc DED processes with a single power source. An industrial-scale component with a mass of 280 kg was built with this process at a high deposition rate close to 10 kg/h, which demonstrated the feasibility of using this process to build large-scale engineering structures with high productivity.
2. Compared to the standard GMA process, the addition of the cold wire in the CW-GMA process led to a change in bead geometry and reduced the remelting and reheating significantly. More specifically, the bead width increases first due to the increase in the melting efficiency and then reaches a plateau due to the energy from the melt pool taken by the cold wire. The remelting reduces constantly with the increase in the CWFS due to the less energy taken by the substrate or pre-deposited layers.
3. The working envelope for the CW-GMA process was achieved based on both single-layer and multi-layer deposition. This can be used to guide the selection of process parameters to avoid any defects in this process. In addition, the process model for multi-layer single-pass walls was achieved, which can be used to predict the geometry features of the deposited walls, including the TWW, EWW and LH.
4. The microstructure and mechanical properties of the CW-GMA was examined and compared to those of the standard GMA process. Due to the addition of cold wire, the specific energy density was reduced in the CW-GMA process compared to that in the standard GMA

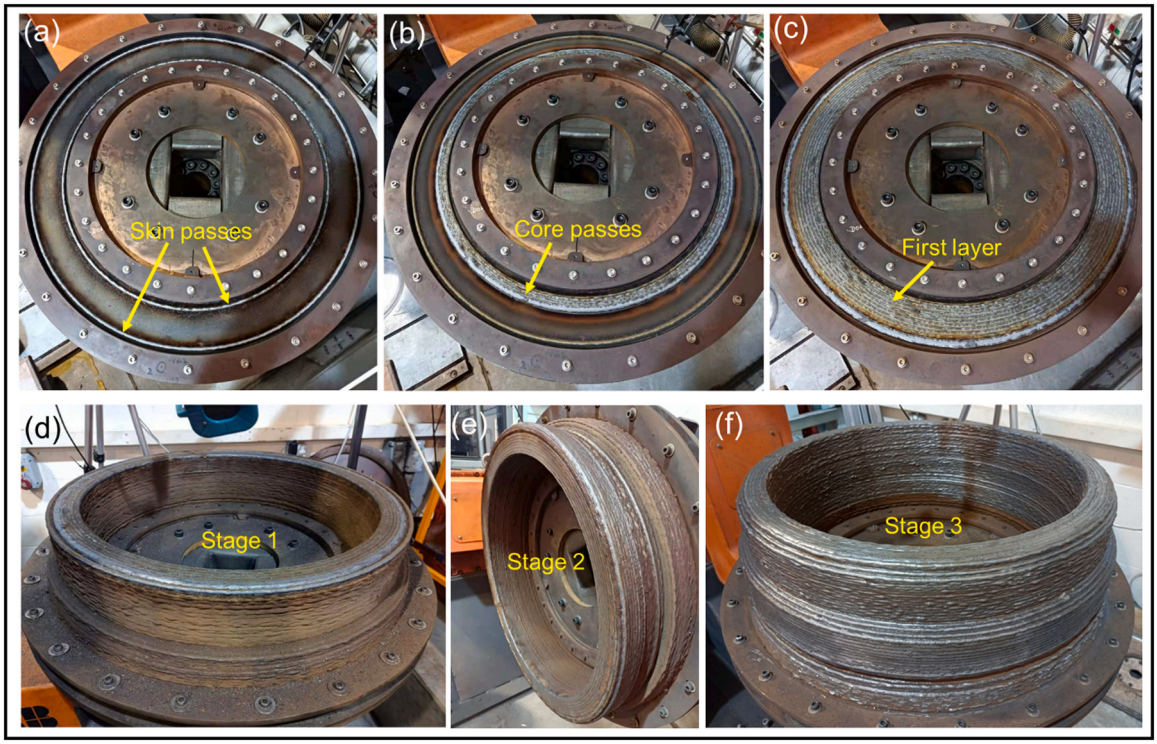

Fig. 16. The deposition process of the component: (a), (b) and (c) shows the deposition of the first layer; (d) shows the deposition of section 1, (e) shows the deposition of section 2, and (f) shows the final appearance of the component.

process, resulting in smaller and more isotropic grains and consequently leading to higher tensile strength with reduced anisotropy in the former process.

CRediT authorship contribution statement

Jialuo Ding: Writing – review & editing, Supervision, Resources, Project administration, Formal analysis. **João Bento:** Methodology, Investigation, Formal analysis. **Jun Wang:** Writing – review & editing, Writing – original draft, Methodology, Investigation, Formal analysis. **Chong Wang :** Writing – review & editing, Writing – original draft, Validation, Methodology, Investigation, Formal analysis, Conceptualization. **Wojciech Suder:** Writing – review & editing, Supervision, Investigation, Formal analysis. **Jian Qin:** Writing – review & editing, Investigation, Formal analysis. **Guangyu Chen:** Writing – review & editing, Investigation, Formal analysis. **Goncalo Pardal:** Writing – review & editing, Methodology, Investigation, Formal analysis. **Stewart Williams:** Writing – review & editing, Supervision, Resources, Funding acquisition, Formal analysis, Conceptualization.

Declaration of Competing Interest

The authors declare that they have no known competing financial interests or personal relationships that could have appeared to influence the work reported in this paper.

Data Availability

Data underlying this study can be accessed through the Cranfield University repository at https://doi.org/10.17862/cranfield.rd.23600214.

Acknowledgement

The authors would like to express their gratitude to Innovate UK (HPWAAM: 53610) and EPSRC (NEWAM: EP/R027218/1) for supporting aspects of this research. The authors would like to thank Dr. Mark Taylor for his contributions in austenite reconstruction. The authors would also like to thank Flemming Nielsen, John Thrower, Nisar Shah, and Steve Pope for the technical support.

Appendix A. Supporting information

Supplementary data associated with this article can be found in the online version at doi:10.1016/j.addma.2023.103681.

References

[1] T. DebRoy, H.L. Wei, J.S. Zuback, T. Mukherjee, J.W. Elmer, J.O. Milewski, A. M. Beese, A. Wilson-Heid, A. De, W. Zhang, Additive manufacturing of metallic components – process, structure and properties, Prog. Mater. Sci. 92 (2018) 112–224, https://doi.org/10.1016/j.pmatsci.2017.10.001.

[2] D. Herzog, V. Seyda, E. Wycisk, C. Emmelmann, Additive manufacturing of metals, Acta Mater. 117 (2016) 371–392, https://doi.org/10.1016/j.actamat.2016.07.019.

[3] D. Jafari, T.H.J. Vaneker, I. Gibson, Wire and arc additive manufacturing: opportunities and challenges to control the quality and accuracy of manufactured parts, Mater. Des. 202 (2021), 109471, https://doi.org/10.1016/j.matdes.2021.109471.

[4] S.W. Williams, F. Martina, A.C. Addison, J. Ding, G. Pardal, P. Colegrove, Wire + arc additive manufacturing, Mater. Sci. Technol. 32 (2016) 641–647, https://doi.org/10.1179/1743284715Y.0000000073.

[5] B. Wu, Z. Pan, D. Ding, D. Cuiuri, H. Li, J. Xu, J. Norrish, A review of the wire arc additive manufacturing of metals: properties, defects and quality improvement, J. Manuf. Process 35 (2018) 127–139, https://doi.org/10.1016/j.jmapro.2018.08.001.

[6] C.R. Cunningham, J.M. Flynn, A. Shokrani, V. Dhokia, S.T. Newman, Invited review article: strategies and processes for high quality wire arc additive manufacturing, Addit. Manuf. 22 (2018) 672–686, https://doi.org/10.1016/j.addma.2018.06.020.

[7] F. Martina, J. Ding, S. Williams, A. Caballero, G. Pardal, L. Quintino, Tandem metal inert gas process for high productivity wire arc additive manufacturing in stainless steel, Addit. Manuf. 25 (2019) 545–550, https://doi.org/10.1016/j.addma.2018.11.022.

[8] C. Petrey, Norsk Titanium charts the future of flight, Modern Metals, August 2018. https://www.modernmetals.com/item/14713-an-additive-manufacturing-technology-undergoes-tests-and-trials-on-numerous-applications-as-it-prepares-for-takeoff.html.

[9] C. Wang, W. Suder, J. Ding, S. Williams, The effect of wire size on high deposition rate wire and plasma arc additive manufacture of Ti-6Al-4V, J. Mater. Process. Technol. 288 (2021), 116842, https://doi.org/10.1016/j.jmatprotec.2020.116842.

[10] C.G. Pickin, S.W. Williams, M. Lunt, Characterisation of the cold metal transfer (CMT) process and its application for low dilution cladding, J. Mater. Process. Technol. 211 (2011) 496–502, https://doi.org/10.1016/j.jmatprotec.2010.11.005.

[11] R.A. Ribeiro, P.D.C. Assunção, E.B.F. Dos Santos, E.M. Braga, A.P. Gerlich, Globular-to-spray transition in cold wire gas metal arc welding, Weld. J. 100 (2021) 121–131, https://doi.org/10.29391/2021.100.010.

[12] R.A. Ribeiro, E.B.F. Dos Santos, P.D.C. Assunção, E.M. Braga, A.P. Gerlich, Cold wire gas metal arc welding: droplet transfer and geometry, Weld. J. 98 (2019) 135S–149S, https://doi.org/10.29391/2019.98.011.

[13] R.A. Ribeiro, P.D.C. Assunção, A.P. Gerlich, Suppression of arc wandering during cold wire-assisted pulsed gas metal arc welding, Weld. World 65 (2021) 1749–1758, https://doi.org/10.1007/s40194-021-01155-7.

[14] R.A. Ribeiro, P.D.C. Assunção, E.B.F. Dos Santos, E.M. Braga, A.P. Gerlich, An overview on the cold wire pulsed gas metal arc welding, Weld. World 64 (2020) 123–140, https://doi.org/10.1007/s40194-019-00826-w.

[15] V.L. Jorge, F.M. Scotti, R.P. Reis, A. Scotti, The effect of pulsed cold-wire feeding on the performance of spray GMAW, Int. J. Adv. Manuf. Technol. 107 (2020) 3485–3498, https://doi.org/10.1007/s00170-020-05247-4.

[16] P.D. Costa Assunção, R.A. Ribeiro, E.B. Emanuel, A.P. Gerlich, E. de Magalhães Braga, Feasibility of narrow gap welding using the cold-wire gas metal arc welding (CW-GMAW) process, Weld. World 61 (2017) 659–666, https://doi.org/10.1007/s40194-017-0466-5.

[17] R.A. Ribeiro, P.D.C. Assunção, E.B.F. Dos Santos, A.A.C. Filho, E.M. Braga, A. P. Gerlich, Application of cold wire gas metal arc welding for narrow gap welding (NGW) of high strength low alloy steel, Materials 12 (2019), https://doi.org/10.3390/ma12030335.

[18] E.S. Costa, P.D.C. Assunção, E.B.F. Dos Santos, L.G. Feio, M.S.Q. Bittencourt, E. M. Braga, Residual stresses in cold-wire gas metal arc welding, Sci. Technol. Weld. Join. 22 (2017) 706–713, https://doi.org/10.1080/13621718.2017.1306014.

[19] L.F.N. Marques, E.B.F. Santos, A.P. Gerlich, E.M. Braga, Fatigue life assessment of weld joints manufactured by GMAW and CW-GMAW processes, Sci. Technol. Weld. Join. 22 (2017) 87–96, https://doi.org/10.1080/13621718.2016.1194735.

[20] J. Stützer, T. Totzauer, B. Wittig, M. Zinke, S. Jüttner, GMAW cold wire technology for adjusting the ferrite–austenite ratio of wire and arc additive manufactured duplex stainless steel components, Metals 9 (2019), https://doi.org/10.3390/met9050564.

[21] H.J. Khaudair, A.A. Ugla, A.R.J. Almusawi, Effect of double wire cold feed on characteristics of additive manufactured components, J. Mater. Eng. Perform. 30 (2021) 6801–6807, https://doi.org/10.1007/s11665-021-06006-6.

[22] C. Wang, Y. Sun, G. Chen, X. Chen, J. Ding, W. Suder, C. Diao, S. Williams, A simplified modelling approach for thermal behaviour analysis in hybrid plasma arc-laser additive manufacturing, Int. J. Heat. Mass Transf. 195 (2022), https://doi.org/10.1016/j.ijheatmasstransfer.2022.123157.

[23] C. Wang, W. Suder, J. Ding, S. Williams, Bead shape control in wire based plasma arc and laser hybrid additive manufacture of Ti-6Al-4V, J. Manuf. Process 68 (2021) 1849–1859, https://doi.org/10.1016/j.jmapro.2021.07.009.

[24] C. Wang, W. Suder, J. Ding, S. Williams, Parametric study of melt pool geometry in hybrid plasma arc-laser melting process for additive manufacturing application, Weld. World (2023), https://doi.org/10.1007/s40194-023-01476-9.

[25] G. Chen, S. Williams, J. Ding, C. Wang, W. Suder, Multi-energy source (MES) configuration for bead shape control in wire-based directed energy deposition (w-DED,), J. Mater. Process. Technol. 304 (2022), https://doi.org/10.1016/j.jmatprotec.2022.117549.

[26] M. Weglowski, Effect of welding current on metal transfer in GMAW, Arch. Mater. Sci. Eng. 33 (2008) 49–56. ⟨http://www.w.archivesmse.org/vol33_1/3318.pdf⟩.

[27] F. Martina, J. Mehnen, S.W. Williams, P. Colegrove, F. Wang, Investigation of the benefits of plasma deposition for the additive layer manufacture of Ti-6Al-4V, J. Mater. Process. Technol. 212 (2012) 1377–1386, https://doi.org/10.1016/j.jmatprotec.2012.02.002.

[28] J. Ding, P. Colegrove, F. Martina, S. Williams, R. Wiktorowicz, M.R. Palt, Development of a laminar flow local shielding device for wire + arc additive manufacture, J. Mater. Process. Technol. 226 (2015) 99–105, https://doi.org/10.1016/j.jmatprotec.2015.07.005.

[29] H. Schleifenbaum, W. Meiners, K. Wissenbach, C. Hinke, Individualized production by means of high power Selective Laser Melting, CIRP J. Manuf. Sci. Technol. 2 (2010) 161–169, https://doi.org/10.1016/j.cirpj.2010.03.005.

[30] C. Wang, W. Suder, J. Ding, S. Williams, Wire based plasma arc and laser hybrid additive manufacture of Ti-6Al-4V, J. Mater. Process. Technol. 293 (2021), 117080, https://doi.org/10.1016/j.jmatprotec.2021.117080.

[31] E. Soderstrom, P. Mendez, Humping mechanisms present in high speed welding, Sci. Technol. Weld. Join. 11 (2006) 572–579, https://doi.org/10.1179/174329306×120787.

[32] T.C. Nguyen, D.C. Weckman, D.A. Johnson, H.W. Kerr, The humping phenomenon during high speed gas metal arc welding, Sci. Technol. Weld. Join. 10 (2005) 447–459, https://doi.org/10.1179/174329305×44134.

[33] X. Meng, G. Qin, Z. Zou, Investigation of humping defect in high speed gas tungsten arc welding by numerical modelling, Mater. Des. 94 (2016) 69–78, https://doi.org/10.1016/j.matdes.2016.01.019.
[34] J. Xiong, G. Zhang, W. Zhang, Forming appearance analysis in multi-layer single-pass GMAW-based additive manufacturing, Int. J. Adv. Manuf. Technol. 80 (2015) 1767–1776, https://doi.org/10.1007/s00170-015-7112-4.
[35] T. Wang, Y.Y. Zhu, S.Q. Zhang, H.B. Tang, H.M. Wang, Grain morphology evolution behavior of titanium alloy components during laser melting deposition additive manufacturing, J. Alloy. Compd. 632 (2015) 505–513, https://doi.org/10.1016/j.jallcom.2015.01.256.
[36] H.Z. Fu, L. Liu, Progress of directional solidification in processing of advanced materials, Mater. Sci. Forum 475–479 (2005) 607–612, https://doi.org/10.4028/www.scientific.net/msf.475-479.607.
[37] H.L. Wei, J.W. Elmer, T. Debroy, Origin of grain orientation during solidification of an aluminum alloy, Acta Mater. 115 (2016) 123–131, https://doi.org/10.1016/j.actamat.2016.05.057.

2023-07-01

A novel cold wire gas metal arc (CW-GMA) process for high productivity additive manufacturing

Wang, Chong

Elsevier

Wang C, Wang J, Bento J, et al., (2023) A novel cold wire gas metal arc (CW-GMA) process for high productivity additive manufacturing, Additive Manufacturing, Volume 73, July 2023, Article Number 103681

https://doi.org/10.1016/j.addma.2023.103681